JMEPEG (2013) 22:3902–3908
DOI: 10.1007/s11665-013-0668-y

1059-9495/$19.00

Characterization of Impact Damage in Ultra-High Performance Concrete Using Spatially Correlated Nanoindentation/SEM/EDX

R.D. Moser, P.G. Allison, and M.Q. Chandler

(Submitted June 20, 2013; in revised form July 24, 2013; published online August 14, 2013)

Little work has been done to study the fundamental material behaviors and failure mechanisms of cement-based materials including ordinary Portland cement concrete and ultra-high performance concretes (UHPCs) under high strain impact and penetration loads at lower length scales. These high strain rate loadings have many possible effects on UHPCs at the microscale and nanoscale, including alterations in the hydration state and bonding present in phases such as calcium silicate hydrate, in addition to fracture and debonding. In this work, the possible chemical and physical changes in UHPCs subjected to high strain rate impact and penetration loads were investigated using a novel technique wherein nanoindentation measurements were spatially correlated with images using scanning electron microscopy and chemical composition using energy dispersive x-ray microanalysis. Results indicate that impact degrades both the elastic modulus and indentation hardness of UHPCs, and in particular hydrated phases, with damage likely occurring due to microfracturing and debonding.

Keywords characterization, EDX, elastic moduli, high performance concrete, nanoindentation, SEM, ultra-high performance concrete

1. Introduction

The ubiquitous use of cementitious materials within protective infrastructures makes quantifying their responses to high strain rate penetration and impact loads a critical need as designs become more reliant on computational tools. Low water-to-cementitious materials ratio (w/cm) reactive powder concretes (ultra-high performance concretes, UHPCs) exhibit superior compressive strength (and ductility when fibers are admixed) compared to conventional concrete and are increasingly being used for high strain rate loading applications (Ref 1). To fully explore the potential of this material for high strain rate loading applications, its fundamental failure mechanisms under impact and penetration loads need to be investigated. UHPCs are a highly heterogeneous material with a w/cm typically less than 0.30 and a microstructure consisting of hydrated cement paste (HCP), unhydrated cement grains, fine aggregates, potentially steel fibers and/or polymer fibers, and pores ranging from nanometer to millimeter in diameter (Ref 2). The addition of pozzolanically reactive silica fume results in an HCP composed primarily of calcium silicate hydrate (C-S-H).

R.D. Moser, P.G. Allison, and **M.Q. Chandler**, Geotechnical and Structures Laboratory, U.S. Army Engineer Research and Development Center, 3909 Halls Ferry Rd., Attn: CEERD-GM-C, Vicksburg, MS 39180. Contact e-mails: Robert.D.Moser@usace.army.mil and paul.g.allison@usace.army.mil.

C-S-H is the most important phase of the Portland cement hydration process and functions as the binding component that holds the various other phases of UHPCs together. C-S-H consists of physically and chemically bound water in nanometer-scale gels, bulk water in gel and capillary pores, adsorbed water on the surfaces of gels, and may behave nano-granularly (Ref 3). Grady (Ref 4) suggests that C-S-H may go through chemical changes such as dehydration or vaporization under shock impact loading.

Instrumented indentation, namely nanoindentation, techniques have been used to quantify the structure-property relationships of concrete at lower length scales. Velez et al. (Ref 5) performed nanoindentation tests to quantify the elastic modulus and hardness of synthetically manufactured Portland cement clinker phases. Hughes and Trtik (Ref 6) used depth-sensing nanoindentation and energy dispersive x-ray (EDX) analysis to correlate the major phase compositions and mechanical properties of HCP. Ulm et al. (Ref 7) developed a novel statistical nanoindentation technique to characterize cement paste and were able to identify the existence of two types of C-S-H, low-density (LD) C-S-H and high-density (HD) C-S-H. Constantinides and coworkers (Ref 8, 9) used a similar approach to study the degrading mechanisms of calcium leaching and high temperature on C-S-H. Sorreli et al. (Ref 10) also used similar techniques to characterize the properties and volume fraction of different phases in UHPCs. Their research showed that UHPCs with a low w/c (0.2) have a much higher volume fraction of HD C-S-H and unhydrated clinker than LD C-S-H compared to concrete with higher w/c. More recent efforts by Chen et al. (Ref 11) have investigated using spatially correlated nanoindentation/scanning electron microscopy (SEM)/EDX techniques similar to those employed herein to investigate the effect of composite formations of C-S-H and $Ca(OH)_2$ on mechanical response measured using nanoindentation.

In this work, the influence of impact loadings on the nanomechanical properties of UHPCs was investigated. Specimens were extracted from impacted and non-impacted panels of UHPC. A novel technique coupling nanoindentation with spatially correlated SEM and chemical analysis using EDX spectroscopy was developed to characterize damage due to high strain rate impact loadings in the UHPC panels. Based on the results of these studies, a possible mechanism for microstructural damage in UHPCs was proposed. Caveats associated with the techniques used are also discussed.

2. Experimental Procedures

2.1 Materials

A UHPC mixture (Baseline Cor-Tuf) with a w/cm of 0.2 and an unconfined compressive strength of 180 MPa was cast into panels 305 mm wide by 305 mm long and 25.4 mm thick for ballistic impact testing. The mixture composition included Class H cement, silica fume, silica flour, siliceous fine aggregate, super plasticizer, and potable tap water. The cast panels underwent a standard high temperature curing process prior to testing. Following the curing process, the panels were impacted by 11-mm-diameter steel spheres at V50, the velocity at which there is a 50% probability of the sphere fully penetrating the panel. V50 values were determined according to MIL-STD-662 (Ref 12).

2.2 Coupled Nanoindentation and SEM/EDX Analysis

Analyses of impacted and non-impacted UHPC specimens were performed using a novel technique of nanoindentation coupled with SEM imaging and EDX chemical analysis. In this coupled method, a large number of indents are performed over a standardized indentation grid placed on the UHPC specimen, after which each indent is spatially correlated using SEM to obtain an image and EDX to determine the chemical composition. The resulting dataset contains the nanomechanical properties and chemical composition along with an image at each indentation site. This coupled method allows for improved differentiation between the various components present in UHPCs and can be used to better correlate alterations in nanomechanical properties (e.g., due to impact loadings) to specific microstructural features. Details on specimen preparation techniques and experimental methods are described below.

2.2.1 Specimen Preparation. Specimens were extracted from the UHPC panel in the impacted zone and a non-impacted zone as shown in Fig. 1. The center of the impacted specimen

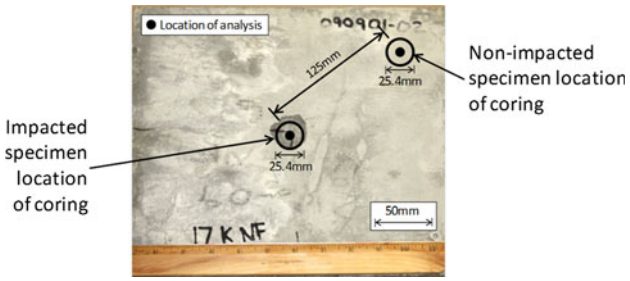

Fig. 1 Location of impacted and non-impacted specimens removed by coring from the RPC panel

location was located within 1 cm of the impacted zone within the impact crater formed by the 11-mm steel sphere. The center of the non-impacted location was 38 mm from both the top edge and side of the panel. This location was selected to minimize the potential for edge effects from casting while also avoiding the damaged zone to the greatest extent. A 25.4-mm-diameter diamond-tipped coring bit was used to core the non-impacted specimens, which were then cast into 31.8-mm-diameter cylindrical molds using EpoHeat low-viscosity epoxy supplied by Buehler. The impacted specimen was sectioned using an oil-cooled Struers Secotom high-precision cut-off saw. The cross section of the specimen was placed into a 31.8-mm-diameter cylindrical mold and mounted in EpoHeat epoxy from Buehler. After the epoxy fully cured, the samples were sectioned in half by the oil-cooled cut-off saw to obtain a cross section from the center of the panel, thus limiting any surface effects such as laitance.

A Buehler Ecomet/Automet 250 automatic polishing wheel was used to polish the extracted specimens. The polishing procedure utilized a 240-grit diamond polishing pad at 230 rpm until the specimen was planar, followed by an UltraPad™ with a 9-μm diamond paste at 130 rpm for 5 min, a TriDent™ pad with a 3-μm diamond paste for 5 min and with a 0.3-μm diamond paste for 5 min, and finally a ChemoMet® pad with 50-nm colloidal silica for 5 min. These polishing steps used a 50:50 mixture of ethylene glycol ($C_2H_6O_2$) and ethanol (C_2H_6O) for a polishing lubricant. All steps used a force of 30 N per specimen for polishing. Once polished, the specimens were stored in a vacuum desiccator prior to testing.

2.2.2 Nanoindentation. Polished specimens were examined using an Agilent Technologies G200 nanoindenter to probe microstructural changes across the surface of impacted and non-impacted regions. Indentation testing was performed using a pyramid-shaped diamond Berkovich indenter with a tip radius of approximately 20 nm. Prior to each measurement, a second-order area function calibration was performed using a fused silica reference material. Load-controlled indentation measurements were performed up to a maximum load of 2 mN at a loading rate of 0.2 mN/s followed by a hold time of 5 s and a 10-s unloading period. A hold segment in air corrected for thermal drift by waiting until the thermal drift was less than 0.5 nm/s before testing commenced.

Prior to performing the nanoindentation experiments, each specimen was examined in the SEM to create a "map" of images approximately 3 mm by 3 mm near the indentation site. This "map" was then used to find a desired location for the indentation grid (i.e., not containing large voids and/or surface defects).

For each specimen, a total of 500 indents were placed with a spacing of 10 μm in the X-direction and 20 μm in the Y-direction. Following the indents performed for nanomechanical measurements, 100-mN fiduciary indents were placed at a spacing of 245 μm in the X-direction and 20 μm in the Y-direction from the first indent to aid in identifying the start, middle, and end of each line of indents so that the indents could be precisely located using the SEM/EDX technique. Assuming a Poisson's ratio of 0.2, mechanical properties such as elastic modulus and indentation hardness were determined for the interaction region of each indentation site.

The Oliver and Pharr (Ref 13) method was used to calculate elastic modulus and indentation hardness at each indent. This method uses the initial unloading portion of the load-displacement curve (Fig. 2) to determine contact stiffness. The hardness, H, and contact stiffness, S, expressions used are

$$H = \frac{P_{\max}}{A}, \quad \text{(Eq 1)}$$

$$S = \beta \frac{2}{\sqrt{\pi}} E_f \sqrt{A}, \quad \text{(Eq 2)}$$

where P_{max} is the maximum load during indentation, A is the contact area, β is a dimensionless correction factor ($\beta = 1.034$ for Berkovich indenter tips), and the effective elastic modulus, E_f, incorporates the elastic displacement occurring for both the specimen and the indenter as

$$\frac{1}{E_f} = \frac{1-\nu^2}{E} + \frac{1-\nu_i^2}{E_i}, \quad \text{(Eq 3)}$$

where the elastic modulus, E, and Poisson's ratio, υ, are for the specimen surface of interest and E_i and υ_i are the elastic modulus and Poisson's ratio of the indenter, respectively.

2.2.3 SEM and EDX Measurements. Specimens were examined both before and after nanoindentation using an FEI Nova NanoSEM 630 variable pressure field emission SEM. Imaging was performed at an accelerating voltage of 10 kV using a backscattered electron (BSE) detector to reveal changes in microstructure and the distribution of phases according to their respective densities. When examined after nanoindentation, the "map" of images was used to generally locate the indentation grid, while the fiduciary indents were used to determine the location of each line of indents such that each indent could be correlated with a location on the image. Point chemical analyses were also performed in conjunction with SEM imaging using a Bruker solid-state EDX detector installed in the FEI SEM. Through proper alignment of the indentation grid facilitated by the fiduciary indents, a standardized point chemical analysis grid was developed that resulted in a dataset of point chemical analyses that were spatially correlated with the location of each indent.

3. Results and Discussion

3.1 Overall UHPC Results

The highly variable phase composition and distribution present in UHPCs present a variety of different nanomechanical properties that were sampled during nanoindentation measurements. Figure 3 shows the load versus depth results of five representative indents corresponding to a fine aggregate, an anhydrous cement grain, hydration products, and an aberrant test. Hydration products were divided into two phases, namely outer (LD) hydration products at a distance from cement grains and inner (HD) hydration products in closer proximity to cement grains, which were determined through molecular simulations and similar nanoindentation studies (Ref 14).

Of particular interest is the faulty or "aberrant" test result shown in Fig. 3, which defies the traditional stiffening indentation curve typical for homogenous interaction regions, but still exhibits an elastic modulus similar to a homogenous phase (in this case inner hydration products). These aberrant tests may present themselves as irregular loading and/or unloading curves (as shown in Fig. 3). In heterogeneous cement-based materials, aberrant test results may also occur due to the presence of voids, polishing defects, cracking during indentation, and as noted more recently, composite or "nanocomposite" multiphase response of material present in the interaction region of the indent (Ref 15-17). The multiphase response of cement-based materials is a topic of recent discussion in the literature and represents an issue that may diminish the utility of nanoindentation as a quantitative microstructural characterization technique. Thus, it is critical to examine each indentation curve and remove aberrant results if reliable quantitative information is desired. All indentation curves in the present study were reviewed and deemed aberrant if they exhibited atypical indentation behavior including the following:

- A non-continuous increase in stiffness observed in the load versus indentation depth curve up to the maximum load, indicating the indent was performed on some type of surface defect such as a void or interface between two phases.
- Large displacements of the indenter in excess of 100 nm with irregular indentation behavior, indicating the presence of a void or microcrack at or in the vicinity of the indentation site.
- Discontinuities in the load versus indentation depth curve, indicating fracture or irregular deformation (e.g., an indent performed on a $Ca(OH)_2$ platelet over an internal microvoid) within the interaction volume of the indent.

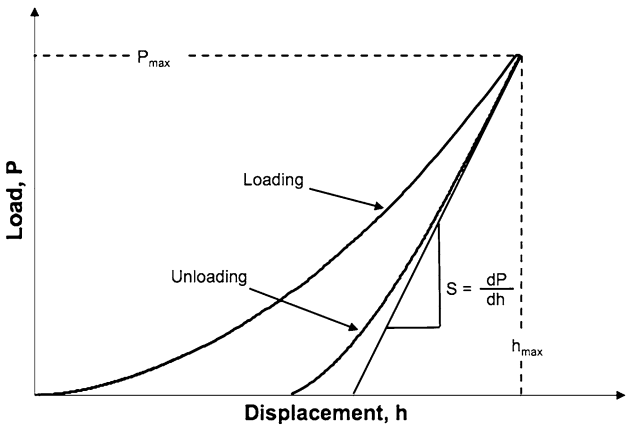

Fig. 2 Schematic of load-displacement curve from nanoindentation with important parameters noted

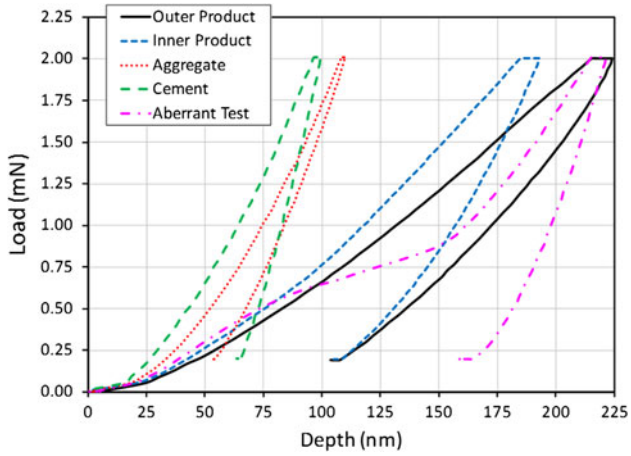

Fig. 3 Typical load vs. indentation depth curves for outer and inner hydration products, aggregate, cement, and an aberrant test result

Based on this assessment, 8% of indents in impacted specimens and 24% of indents in non-impacted specimens were deemed aberrant and removed from the dataset.

Figure 4(a) illustrates a typical grid of 500 measurement indentation points and fiduciary indents superimposed on a BSE micrograph of an UHPC specimen. Using BSE imaging, the anhydrous cement and silica fume can be seen with a bright signature, followed by fine aggregates and silica flour, and finally by the HCP (i.e., solid products of cement hydration with low density) and voids that appear darkest in the image. The HCP appeared to be composed primarily of C-S-H, with all $Ca(OH)_2$ likely consumed by pozzolanic reactions and subsequently converted into supplementary C-S-H. Figure 4(b) and (c) presents contour maps of Ca:Si ratio and elastic modulus results, respectively, corresponding to the indentation grid shown in Fig. 4(a). A clear correlation can be observed between the location of the various components of the UHPC and their respective chemical composition and mechanical properties.

The benefits of using this coupled nanoindentation/SEM/EDX technique are particularly apparent when trying to

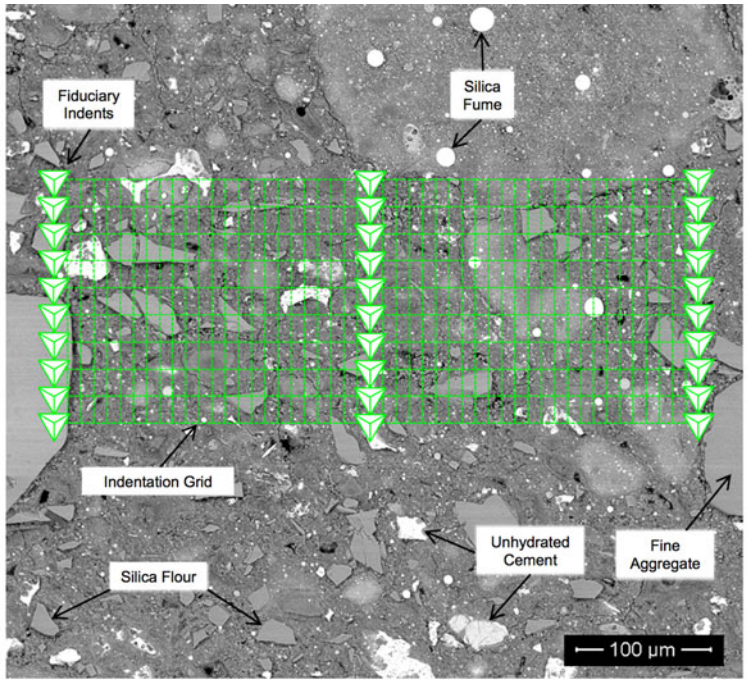

(a) SEM-BSE micrograph of typical reactive powder concrete microstructure with measurement indentation grid and fiduciary indents superimposed.

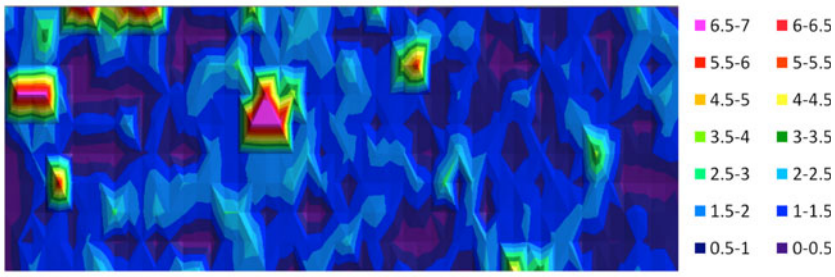

(b) Map of Ca:Si corresponding to indentation grid.

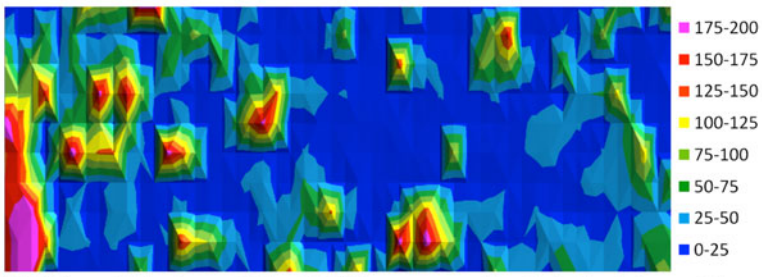

(c) Map of elastic modulus (GPa) corresponding to indentation grid.

Fig. 4 Typical results from coupled nanoindentation and SEM/EDX studies performed on UHPC specimens. (a) SEM-BSE micrograph of typical UHPC microstructure with measurement indentation grid and fiduciary indents superimposed. (b) Map of Ca:Si corresponding to indentation grid. (c) Map of elastic modulus (GPa) corresponding to indentation grid

differentiate between phases with similar properties. For example, fine aggregate particles and anhydrous cement present in low w/c concretes may exhibit similar mechanical properties, which make phase identification/quantification from only nanoindentation results a challenging task. However, when nanoindentation measurements are coupled with chemical composition at the indentation site, the distinction between fine aggregates (with low Ca:Si approaching zero) and cement (with high Ca:Si of 5-7) becomes clear. Similar comparisons can be made for the various phases of cement hydration present in the HCP.

Another feature of the nanoindentation measurements clearly shown in the elastic modulus contour map in Fig. 4(c) is the gradual transition in nanomechanical properties present at interfaces between two phases. This behavior is the result of a composite response of material present within the interaction region below each indent as discussed above.

With the aberrant results removed from the dataset, further analyses of "valid" nanoindentation results were performed. Figures 5 and 6 present histograms of the elastic modulus and hardness results of all "valid" indents performed on non-impacted and impacted specimens in the present study. Results presented in Fig. 5 encompass those of anhydrous cement, siliceous fine aggregates, silica flour, the HCP (primarily composed of C-S-H), and voids/porosity. Impacted specimens exhibited a mean elastic modulus of 47.9 GPa compared with 76.7 GPa in non-impacted specimens. In particular, significant reductions in the proportion of indents with elastic moduli between 60 and 110 GPa were observed in impacted specimens, a range common for silica flour and siliceous fine aggregates (Ref 10, 17). These results only represent analyses performed at discrete sites at different radii from the impact site (i.e., impacted and non-impacted zones). Damage is anticipated to decrease as the radial distance from the crater in the impacted zone increases.

The effect of impact (Fig. 6) was much more pronounced in hardness measurements, where a large shift in hardness from a mean of 6.3 to 2.7 GPa was observed. In impacted specimens, there was a particularly high increase in the proportion of

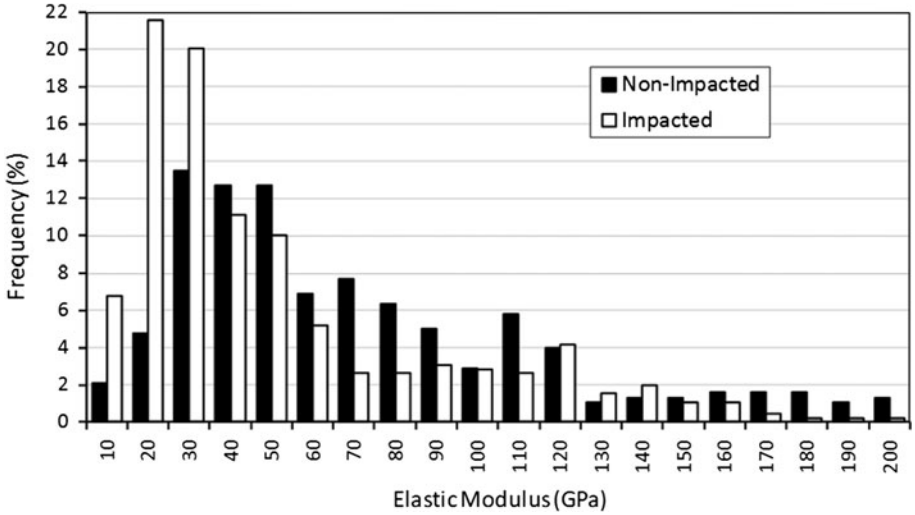

Fig. 5 Histogram of elastic modulus results from nanoindentation experiments performed on non-impacted and impacted RPC specimens

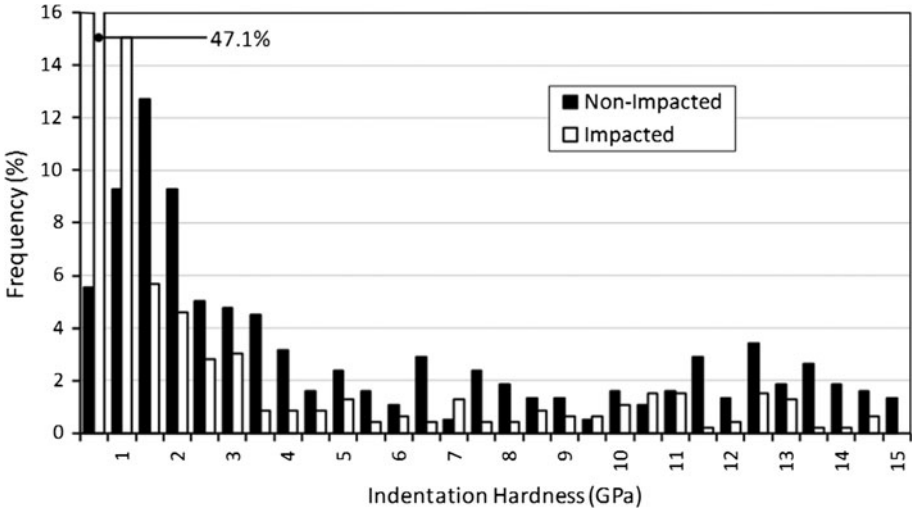

Fig. 6 Histogram of indentation hardness results from nanoindentation experiments performed on non-impacted and impacted RPC specimens

indents with hardness between 0.5 and 1.5 GPa associated with a reduction in the proportion of indents with hardness above 4 GPa. Similar to the elastic modulus results, the effect of the impact and subsequent damage is anticipated to decrease further from the impacted zone.

While removal of seemingly aberrant test results did improve the quality of results included in the dataset for analysis, measured mechanical properties presented in Fig. 5 and 6 indicate values of elastic modulus and hardness that are not theoretically probable (i.e., elastic modulus in excess of 150 MPa) in typical UHPCs or mortars containing HCP and fine aggregates. Such behavior is supported by recent observations of "spurious peaks" that may correspond to surface defects or the presence of multiple hydration products present within interaction volume of the indent (Ref 17). This observed behavior in spatially correlated nanoindentation/SEM/EDX measurements reduces the validity of nanoindentation for determining single-phase nanomechanical properties.

3.2 Results from Hydrated Phase Fraction

While these nanoindentation results suggest that impact loadings have a significant influence on both the elastic modulus and hardness of UHPCs, it is difficult to determine by what possible mechanism degradation occurs. In order to further evaluate the possible mechanisms causing the observed degradation in nanomechanical properties, indents likely associated with homogenous regions of hydrated phases were extracted from the full dataset of non-impacted and impacted UHPC specimens. Indents identified as hydrates were selected based on a Ca:Si between 0.5 and 2 (consistent with typical C-S-H) with an elastic modulus between 10 and 50 GPa (range typical for outer and inner product C-S-H (Ref 10, 11)). Out of each dataset, approximately 10% of the indents were deemed as hydrates. Ca:Si ratios of the hydrated phases' sub-dataset were 1.44 and 1.42 for non-impacted and impacted specimens, respectively, indicating that the method was successful in identifying regions that contained hydrates of similar chemistry before and after impact.

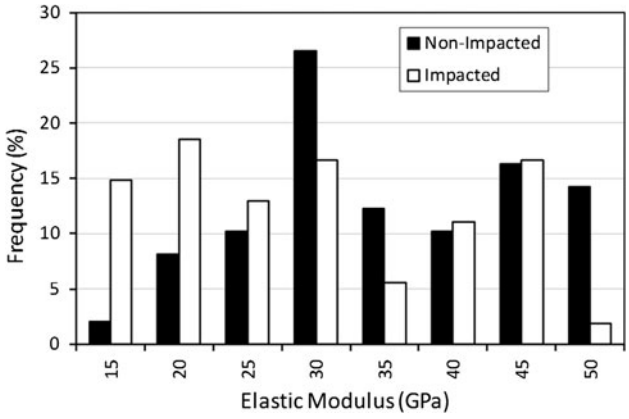

Fig. 7 Hydrated phase fraction elastic modulus of impacted and non-impacted specimens

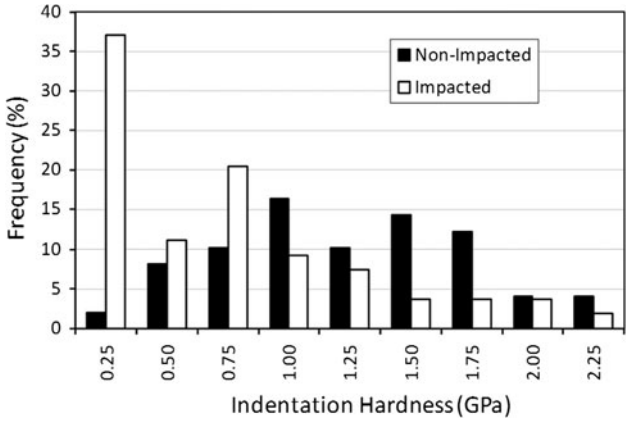

Fig. 8 Hydrated phase fraction indentation hardness of impacted and non-impacted specimens

The histograms shown in Fig. 7 and 8 depict the distribution in elastic modulus and indentation hardness of hydrated phases for non-impacted and impacted specimens. Hydrated phases present in non-impacted specimens exhibited a mean elastic modulus of 32.5 GPa and mean indentation hardness of 1.56 GPa. C-S-H present in impacted specimens exhibited a mean elastic modulus of 27.4 GPa and mean indentation hardness of 0.66 GPa, with a significant increase in hardness between 0.25 and 0.75 GPa.

These reductions in elastic modulus and, in particular, hardness in impacted samples suggest that the hydrate fraction of the cement paste, in addition to the overall microstructure of UHPCs, is degraded under high strain rate impact loadings. The dehydration/vaporization mechanism proposed by DeJong and Ulm (Ref 9) was shown as a possible deterioration mechanism resulting in decreased C-S-H packing factors and in turn reduced elastic modulus and hardness as measured by nanoindentation. However, unless additional secondary chemical bonding was to occur between C-S layers (similar to irreversible creep mechanisms (Ref 15) during the vaporization event), it is likely that rehydration of the hydrates would occur slowly. Furthermore, if such bonding were to occur, densifying the paste fraction and limiting rehydration, the elastic modulus and hardness would likely increase rather than decrease. Based on the results presented in Fig. 5 and 6, it is clear that the majority of degradation in the UHPC indentation dataset is associated with reductions in elastic modulus and hardness associated with inert particles and unhydrated cement. Therefore, it is likely that the majority of degradation in UHPCs following impact loading results from microfracturing and/or debonding. Recent research efforts determined similar damage mechanisms using petrographic analyses and x-ray diffraction, which have evidenced microfracturing and debonding as well as pressure- and temperature-induced phase changes in siliceous aggregates and silica flour in the impacted region (Ref 16).

4. Conclusions

A novel statistical nanoindentation technique was developed that spatially correlated the location of a large statistical indentation grid on an image obtained using BSE-SEM and chemical analyses using EDX. The limitations of these techniques must be understood as they can only be used to infer information related to micro- and nanostructural alterations resulting from impact. Direct measurements of structure (e.g., x-ray diffraction, nuclear magnetic resonance spectrometry) would be necessary to further elucidate changes occurring

at lower length scales following impact. Nonetheless, this coupled nanoindentation/SEM/EDX technique does present a unique approach to evaluate the nanomechanical properties and their spatial distribution in heterogeneous materials such as UHPC. Using this method, the influence of high strain rate impact loadings on the nanomechanical properties of UHPCs was determined. Significant degradation in both the elastic modulus and hardness occurred due to impact loadings of UHPCs. Closer examination of hydrated phases also showed degradation. However, a link between chemical changes in the hydrated phase fraction and deterioration in nanomechanical properties could not be made. Based on analyses of all indents performed on UHPC specimens, it is likely that much of the observed degradation in elastic modulus and hardness stems from microfracturing and debonding, which occurs due to the impact.

Future work involves additional experimental studies and quantitative data analyses to further evaluate the possible mechanisms of degradation present in UHPC. New in-situ nanoindentation measurement techniques are also being investigated to improve the correlation between the desired phase being indented and its nanomechanical properties as well and elucidating the interaction between the indenter and the polished cement past surface.

Acknowledgments

The authors would like to thank Dr. Todd Rushing of the Geotechnical and Structures Laboratory, US Army Engineer Research and Development Center (ERDC), for supplying the specimens for this study. Financial support for this work was provided by the ERDC and the U.S. Department of Defense SMART Scholarship Program. Permission to publish was granted by the Director, ERDC Geotechnical and Structures Laboratory.

References

1. S.G. Millard, T.C.K. Molyneaux, S.J. Barnett, and X. Gao, Dynamic Enhancement of Blast-Resistant Ultra High Performance Fibre-Reinforced Concrete Under Flexural and Shear Loading, *Int. J. Impact Eng.*, 2010, **37**(4), p 405–413
2. T.S. Rushing, N. Boone, A. Irizzary, and R. Magee, Independent Effects of Matrix Strength and Fiber Reinforcement on Concrete's Ballistic Resistance, *Proceedings of the 80th Shock and Vibration Symposium* (San Diego, CA, USA), 2009
3. G. Constantinides and F.J. Ulm, The Nanogranular Nature of C-S-H, *J. Mech. Phys. Solids*, 2007, **55**(1), p 65–90
4. D. Grady, Shock Equation of State Properties of Concrete, *Proceedings of Structures Under Shock and Impact IV* (Southampton, UK), 1996, p 405–414
5. K. Velez, S. Maximilien, D. Damidot, G. Fantozzi, and F. Sorrentino, Determination by Nanoindentation of Elastic Modulus and Hardness of Pure Constituents of Portland Cement Clinker, *Cem. Concr. Res.*, 2001, **31**(4), p 555–561
6. J.J. Hughes and P. Trtik, Micro-Mechanical Properties of Cement Paste Measured by Depth-Sensing Nanoindentation: A Preliminary Correlation of Physical Properties with Phase Type, *Mater. Charact.*, 2004, **53**(2–4), p 223–231
7. F.J. Ulm, M. Vandamme, C. Bobko, J.A. Ortega, K. Tai, and C. Ortiz, Statistical Indentation Techniques for Hydrated Nanocomposites: Concrete, Bone, and Shale, *J. Am. Ceram. Soc.*, 2007, **90**(9), p 2677–2692
8. G. Constantinides and F.J. Ulm, The Effect of Two Types of C-S-H on the Elasticity of Cement-Based Materials: Results from Nanoindentation and Micromechanical Modeling, *Cem. Concr. Res.*, 2004, **34**(1), p 67–80
9. M.J. DeJong and F.J. Ulm, The Nanogranular Behavior of C-S-H at Elevated Temperatures (Up to 700 °C), *Cem. Concr. Res.*, 2007, **37**(1), p 1–12
10. L. Sorreli, G. Constantinides, F.J. Ulm, and F. Toutlemonde, The Nano-Mechanical Signature of Ultra-High Performance Concrete by Statistical Nanoindentation Techniques, *Cem. Concr. Res.*, 2008, **38**(12), p 1447–1456
11. J.J. Chen, L. Sorreli, M. Vandamme, F.J. Ulm, and G. Chanvillard, A Coupled Nanoindentation/SEM-EDS Study on Low Water/Cement Ratio Portland Cement Paste: Evidence for C-S-H/Ca(OH)2 Nanocomposites, *J. Am. Ceram. Soc.*, 2010, **93**(5), p 1484–1493
12. MIL-STD-662F, Military Standard: V50 Ballistic Test for Armor, 1997
13. W.C. Oliver and G.M. Pharr, An Improved Technique for Determining Hardness and Elastic Modulus Using Load and Displacement Sensing Indentation Experiments, *J. Mater. Res.*, 1992, **7**(6), p 1564–1583
14. D. Davydov, M. Jirasek, and L. Kopecky, Critical Aspects of Nano-Indentation Technique in Application to Hardened Cement Paste, *Cem. Concr. Res.*, 2011, **41**(1), p 20–29
15. P.K. Mehta and P.J.M. Monteiro, *Concrete: Microstructure, Properties, and Materials*, McGraw-Hill Companies Ltd., New York, 2006
16. F. Ren, C. Mattus, J. Wang, and B. DiPaolo, Microstructural Characterization of UHPC Materials Subject to Impact Testing and Heating, *2nd Annual Meeting on Advances in Cement-Based Materials* (Nashville, TN, USA), 2011
17. P. Trtik, B. Munch, and P. Lura, A Critical Examination of Statistical Nanoindentation on Model Materials and Hardened Cement Pastes Based on Virtual Experiments, *Cem. Concr. Compd.*, 2009, **31**(10), p 705–714